clinically important. Of these, 17 (8.1%) were detected during anaerobic incubation and 43 (20.8%) were detected during aerobic incubation. The rest of the isolates (150) were detected during both aerobic and anaerobic incubation.

(Table 1) Isolates That Only Grew In Anaerobic Blood Culture Bottles

Faculatative Anaerobes	Obligate Anaerobes
Lactobacillus sp. (2)	Bacteroides sp. not fragilis (1)
Staphylococcus aureus (2)	Bacteroides fragilis (1)
Escherichia coli (4)	Bacteroides fragilis species (1)
Pseudomonas aeruginosa (1)	Peptostreptococcus (1)
Streptococcus agalactiae (1)	
Enterococcus faecalis (1)	
Escherichia fergusonii (1)	
Citrobacter freundii (1)	

Conclusions: It would not be clinically safe or cost effective to eliminate anaerobic blood culture bottles. We would have missed 17 clinically important bacteremias (8.1%) that could have harmed patients and led to overall higher costs. In this study, predominately facultative anaerobes were isolated from the anaerobic blood culture bottles (13 of 17). The BD BACTEC Lytic/10 Anaerobic/F Culture Vials system used at our institution utilizes .26% saponin, a detergent that lyses red and white blood cells, enabling the recovery of some bacteria that would not have grown in aerobic culture bottles.

Informatics

1439 Evaluation of Microvessel Density Using Light Microscopy Versus Computerized Image Analysis in Multiple Myeloma.

N Aboud, TW Kelley, JR Jacobsen, S Tripp, A Wilson, R Fenn, SL Perkins, ME Salama. ARUP Reference lab, salt lake city; University of Utah, Salt Lake city; St. Jude Children's Research Hospital, Memphis.

Background: Emerging data suggest a prognostic value of angiogenesis in bone marrow in Multiple Myeloma (MM). However, most of studies used a quantitative evaluation of the microvessel density using a method, so-called hot-spot technique that was developed for characterization of angiogenesis in solid tumors. Given that solid neoplasms and the bone marrow have differences regarding the vascular structures and the distribution of microvessels, we evaluated performance of microvessel count done manually on light microscopy (MVP) and microvessel parameters obtained using computerized image analysis in the context of other prognostic and microenvironment factors.

Design: MM cases diagnosed in 2007-2008 with adequate materials were included in the study. Immunohistochemical stains for CD138 and CD34 were performed to highlight Plasma cells (PC) and vasculature, respectively. Adequately CD34 & CD138 stained bone marrow core biopsies were digitally scanned with the ScanScope® XT system (Aperio Technologies, Inc., Vista, CA) and areas with most abundant PC were analyzed via 'microvessel density algorithm. Parameters obtained from the algorithm including microvessel density (MVD), vessel perimeter (VP), total number of vessels (TV) and segments with vessels of various bin areas (0-15, 15-30, 30-50, 50-75, 75-100, and 100um^2 increment up to 900 um^2) were analyzed with regards to association / prediction of PC and other prognostic / microenvironment parameters. All statistical analyses were performed using SAS software, Version 9.1 of the SAS System.

Results: 46 patients (29 M) ranged in age between 41-78 y were included. Immunoglobulin subtypes and microenvironment parameters including mast cells & trabecular volume didn't correlate with PC. Microvessel density as measured by MVP, MVD, or TV, correlated significantly with the PC with p values of <.0001, 0.0018 and 0.006, respectively. MVP showed higher Pearson ranking as compared to VP and TV at 0.56, 0.45 and 0.40, respectively. MVD was the most tightly correlated parameter with disease stage. When ranked for predictive power for plasma cell number, the segment of blood vessel with cross-area of 400-500 um^2 ranked higher for prediction of PC.

Conclusions: Both MVP and MVD significantly correlate with plasma cell number. MVP was the highest predictor according to Pearson correlation. MVD correlated better with the stage of the disease. Vessels within 400-500 um^2 segment ranked the highest in predicting plasma cells number.

1440 Google Earth and Panoramic Photo Software in the Management of Virtual Slides.

L Alfaro, E Poblet, MJ Roca, P Catala, A Navea. Fundacion Oftalmologica del Mediterraneo, Valencia, Spain; Albacete University, Spain; Hospital Arnau de Vilanova, Valencia, Spain.

Background: Virtual slides are high resolution scanned images obtained from glass slides, and stored in a multi-layered pyramidal file format to allow review at computer screens with quick "zoom in" and "drag" along the image, simulating an optical microscope. Virtual microscopy has greatly developed; however, high prices of scanners and software have hindered a much broader implementation. We have tested the use of free and low cost software to overcome these limitations. Google Earth and diverse panoramic photo software share with virtual microscopy the fact of using image zooming and dragging. They seem suitable to be adapted for virtual slides.

Design: Ten slides from the files of our hospital with samples of different size and shape were retrieved. Two scanners were used to obtain virtual slides, a Mirax Midi (Zeiss) and an Aperio XT. Scanned files with .mrxs and .svs specific extensions were exported to conventional .tiff and .jpg files. New images with pyramidal structure were generated for Google Earth, Zoomify, HD View, Silverlight Deep Zoom, and Gigapan. Images were hosted in two servers, a commercial hosting server (http://e-pat-org/vs/COMP), and a portable USB hard drive with Apache server software.

Results: All five software options allowed the display of the virtual slides without limitations for diagnostic purposes. Some advantages and minor differences between programs were mainly found regarding conversion processes from the original slides. Google Earth showed a good display, but a slower pyramidal structure creation when using big size samples (i.e. 2 x 2 cm) with the generators used (Map Tiler, and Google Earth Photo Overlay Creator). Zoomify, which is based on Flash, had a slightly less soft transition between fields, but a higher compatibility, and an excellent viewer to compare two different images. HD View had the fastest converter, and a very good quality, but a specific plug-in was required. Silverlight Deep Zoom had also a clean transition between fields but the converter (Deep Zoom Composer) showed incompatibilities with .tiff files using JPEG compression. The major limitation of Gigapan is that files have to be hosted at Gigapan server.

Conclusions: Free and low cost software for virtual microscopy is available with no need of high computer knowledge, and is highly suitable to establish compatibility between different virtual microscopy devices.

1441 Direct Digital Imaging of Breast Tissue Using Spectral-Domain Optical Coherence Tomography.

JL Fine, L Kagemann, G Wollstein, H Ishikawa, JS Schuman. University of Pittsburgh, PA.

Background: Spectral-domain optical coherence tomography (OCT) permits direct imaging of tissue in 3D, potentially bypassing glass slide workflow. Other specialties are developing in-vivo microscopic imaging using OCT and other techniques. This represents a challenge and an opportunity; we can begin augmenting traditional histology and pathology with 3D-derived information. Here we correlated OCT images with H&E images of breast tissue.

Design: OCT images were acquired from formalin-fixed, paraffin-embedded tissue blocks representing normal breast, papilloma, DCIS, invasive ductal carcinoma, and axillary lymph node with small tumor deposits (Bioptigen, Research Triangle, North Carolina, USA). 2 mm deep volumes of tissue were sampled with 500 x 500 x 1024 voxel resolution over small areas of the block (transverse resolution 20 microns, axial resolution 2 microns). OCT images underwent post-processing then were correlated with routine H&E stained slides. Virtual slices, 3D reconstructions and animations were created.

Results: Features such as fat vacuoles, vessels, and tissue outlines were readily identified, as were some normal ducts. Ducts involved by DCIS were easily recognized when surrounded by fat; comedo necrosis (*) was faintly visible.

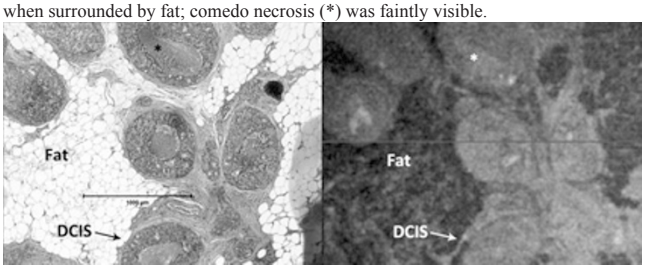

Benign breast ducts and lobules were subtle, seen as slight shadows in the image with a larger duct structure. Invasive carcinoma was also subtle but had a discernable texture. Lymph node scans were matched with H&E but details were difficult to see due to low contrast.

Conclusions: This was an effort to begin delineating 3D histology and pathology of breast tissue using direct tissue imaging by OCT. Contrast and resolution are currently less than that available from glass microscopy, but potential exists for improving scan quality and for extracting more information from images (ie development of image analysis and better post-processing technique). Other specialties are now developing in-vivo microscopic tests that generate similar 3D histological images. In addition to potentially bypassing or reducing reliance on glass microscope slides, "virtual biopsy" expertise may soon be in demand by clinicians and may potentially represent a new discipline within Anatomic Pathology.

1442 The Utility of Dynamic Passive Telepathology in Neuropathology Intraoperative Consultations: A Critical Evaluation of Cytologic and Frozen Section Preparations.

M Gokden, SG Sharma, AG Saad. University of Arkansas for Medical Sciences, Little Rock; Arkansas Children's Hospital, Little Rock.

Background: Telepathology (TP) is becoming widely used especially in institutions where access to subspecialty expertise is limited. TP have been previously studied in intraoperative consultation (IOC) in neuropathology (NP), but its utility in smear preparations in NP is not well defined. We analyzed the utility of TP in NP with respect to neoplasm types, as well as the cytologic (C) and frozen section (FS) components.

Design: Total of 72 consecutive cases {43 gliomas of various histologic types and grades, 10 meningiomas, 4 lymphoid processes, 4 peripheral nerve sheath tumors (PNST), 8 metastatic carcinomas, 3 nondiagnostic cases} with available C & FS slides, were identified retrospectively from the files in 2009-2010. The TP System comprised of Nikon Digital Sight DS-L2 & Nikon Eclipse 55i microscope. It was operated by the neuropathologist (NPst) at the primary center while the NPst at the remote location reviewed the real-time images on a computer screen. Both were blinded to the final diagnoses and made independent diagnoses. The evaluation started with cytologic component and was limited initially to morphology; clinical & radiologic data were made available as requested. C & FS components were timed separately. The time used and concordance rates were analyzed; any practical issues were discussed.

Results: Average time for C/FS in seconds were: Glioma 48/69; lymphoid 54/67; metastatic carcinoma 58/49; PNST 52/109; meningioma 29/84; nondiagnostic 22/55;

entire group 44/72 (range 10-209/24-376). There were no discrepancies between the two NPst in C or FS components. There were 11 discrepancies between IOC diagnoses and final diagnoses on permanent sections, mainly due to high grade-low grade discrepancy of gliomas. These were due to sampling variation. More importantly, no discrepancies occurred between the study and the actual IOC diagnoses.

Conclusions: TP proved to be highly efficient in C and FS component of NP IOC with high degree of concordance between the two NPst. It was felt that the operator's experience at the primary site is crucial for the speed and accuracy of the results by rapidly finding and displaying the diagnostically important fields, and by selecting and providing the critical clinical and radiologic information. In addition, TP can be utilized by those who practice IOC based only on cytologic evaluation.

1443 Quantifying Tumor Infiltrating Lymphocytes in Ovarian Cancer TMAS.

A Janowczyk, S Chandran, M Feldman, A Madabhushi. IIT Bombay, Mumbai, India; UPenn, Philadelphia; NJ Rutgers, New Brunswick.

Background: Research has shown that the presence of lymphocytes within tumor cells (tumor infiltrating lymphocytes (TILs)), is reflective of outcome for Ovarian Cancer (OCa). Hence, is it important to distinguish between TILs and lymphocytes that reside in the stroma (non-TILs). Manually counting TILs is tedious and time consuming, thus there is a clear need for automation. Standard computer vision approaches are not only computationally expensive, but fail to account for subtle differences in local structural morphology (TILs are densely surrounded by tumor cells, non-TILs are not). We present a novel local morphologic scale (LMS) descriptor which quantitatively captures local structure. Morphologic features derived from LMS can be used to train a supervised classifier to distinguish between stroma and tumor regions, and thus TILs and non-TILs.

Design: The algorithm is as follows: Identify all lymphocytes from a stained OCa TMA using Hierarchical Normalized Cuts (HNCut), a minimally interactive object detection scheme. Next we generate LMS signatures (Figures 1 (b), (d)) for regions surrounding each lymphocyte. This signature is determined by sampling the path of "particles", which are adjusted based on a simple physics model, as they leave the region. Features (such as length of LMS path) at each location can then be extracted and used to train a classifier to distinguish between TILs and non-TILs.

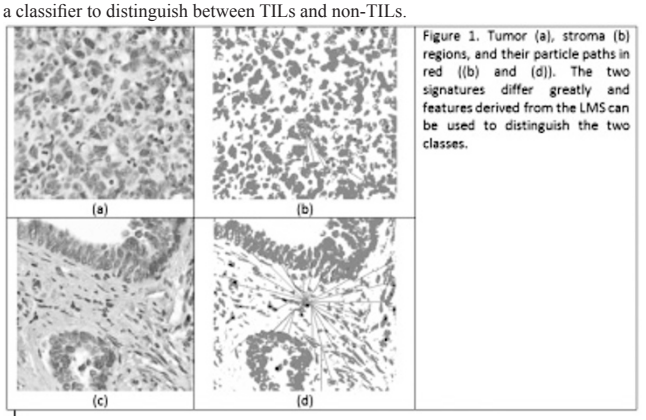

Figure 1. Tumor (a), stroma (b) regions, and their particle paths in red ((b) and (d)). The two signatures differ greatly and features derived from the LMS can be used to distinguish the two classes.

Results: 16 TMA cylinders across 6 different OCa studies were used to evaluate the LMS algorithm against a pathologist's annotation of what constituted a TIL. The LMS classifier was employed to identify TILs within a total of 8000 200X200 image patches. A Probabilistic Boosting Tree was trained using LMS features to distinguish between TILs and non-TILs using 80% of the data, the remaining 20% being used for evaluation. Average ROC AUC was .803.

Conclusions: We presented a novel, local, morphologic image descriptor (LMS) that was successfully applied to rapidly and automatically discriminate TILs and non-TILs on OCa TMAs. In future work we intend to apply LMS to identifying TILs in the context of other diseases (e.g. Her2+ breast cancers).

1444 Computer-Based Classification of Nuclei in Gliomas.

J Kong, LAD Cooper, CS Chisolm, F Wang, CS Moreno, T Kurc, DJ Brat, JH Saltz. Emory University, Atlanta, GA.

Background: We are conducting computer-based morphological studies of diffuse gliomas to identify morphological correlates of patient outcome and genomic characterizations. Previous work using The Cancer Genome Atlas glioblastoma data demonstrated morphological differences between tumors of specific transcriptional classes when averaged nuclear features within a tumor are examined. In this study we subclassified different types of cell nuclei encountered in gliomas using machine-based algorithms in an effort to increase the resolution of correlative morphological investigations.

Design: We used a set of 16 digitized H&E-stained images to collect neuropathologists' classifications of 2240 nuclei as neoplastic astrocytes, neoplastic oligodendrocytes, reactive endothelial cells, reactive astrocytes, and hematoxylin-stained debris. The slides were chosen from a spectrum of gliomas, including astrocytomas, oligodendrogliomas, oligoastrocytomas, and glioblastomas (which contained 0+,1+,2+ oligo component). Nuclei in these images were segmented using computer algorithms. A set of features describing nuclear shape, texture and cytoplasmic staining was calculated to describe each nucleus. Features derived from the neuropathologist-classified nuclei were used to train a computer classification system. A feature selection algorithm first identified a subset of features that best captures class differences. Selected features were then used to train a quadratic discriminant classifier. A five-fold cross validation was used to calculate the average classification accuracy as the ratio of the number of correctly classified nuclei to that of total nuclei. The bottom 10% of ambiguous nuclei as ranked by classification confidence score were discarded from each fold.

Results: We found that the overall computer-based classification accuracy was 92%. The classifier achieves promising accuracy for neoplastic oligodendrocytes (95.6%), neoplastic astrocytes (91.9%), reactive endothelial cells (89.0%), and debris (89.9%). Reactive astrocytes (85.6%) are the most difficult to classify, with 5.3% being mislabeled as neoplastic astrocytes and 6.2% being misclassified as reactive endothelial cells.

Conclusions: These results suggest that computational morphometry can achieve reasonable classification rates for multiple nuclear classes commonly encountered in the gliomas. We are currently extending the classification scheme to include microglia, mitotic figures, and the normal nuclear types that are critical for studies on low-grade gliomas.

1445 Fusion of Proteomic and Histologic Image Features for Predicting Prostate Cancer Recurrence after Radical Prostatectomy.

G Lee, S Doyle, J Monaco, M Feldman, JE Tomaszewski, SR Master, A Madabhushi. Rutgers University, Piscataway; University of Pennsylvania, Philadelphia.

Background: An estimated 30% of prostate cancer (CaP) patients suffer biochemical failure (BcF) within 10 years following radical prostatectomy. While Gleason grade is currently the best predictor of CaP aggressiveness, in several instances grade alone is unable to identify candidates for BcF. Mass spectrometry (MS) methods have recently been shown to yield predictive protein biomarkers for identifying candidates at risk for BcF. However, neither MS nor Gleason grade by itself constitutes a sufficiently strong predictor for CaP recurrence. Since the histologic image and proteomic attributes represent orthogonal sources of information, combining the channels of data could yield a new fused, feature space that can be used to identify patients at risk for CaP recurrence. However, data fusion methods for combining multi-scale, multi-modal, imaging and non-imaging data are not extant. In this work we present a novel machine learning scheme for quantitatively fusing histologic image and proteomic attributes for developing a meta-classifier for identifying candidates for BcF.

Design: Quantitative descriptors of gland morphology and nuclear architecture are computed from the digitized CaP histology. Peptide measurements are performed via MS at the site of the dominant nodule on the histology. Novel image and proteomic feature extraction tools are applied to extract quantitative data from a cohort of 19 patients (10 who were relapse free and 9 who had BcF). Our data fusion scheme was then applied to combine the image and proteomic signatures.

Results: The improved separation in the fused representation in Figure 1 is supported by classification accuracy using a Random Forest classifier, showing 39% classification accuracy on the morphological image descriptors, 43% on the architectural image descriptors, 84% on the protein features, and 86% on the fused data representation.

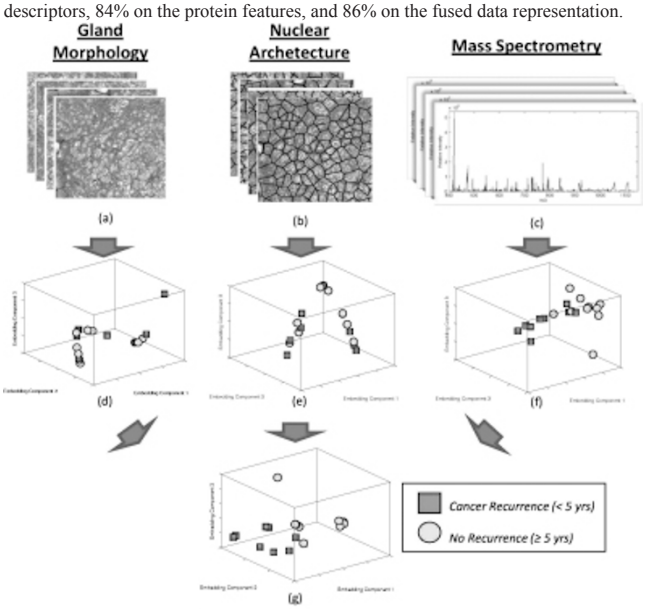

Figure: CaP patients (d-f) are represented by (a) Morphological image Descriptors, (b) Architectural image Descriptors, and (c) Protein features respectively. Improved separation between CaP recurrence/non-recurrence cases can be seen in the fused representation in (g).

Conclusions: We presented a fused histology, proteomic biomarker for identifying radical prostatectomy patients who are at risk for BcF. This fused classifier outperformed Gleason grade and MS derived protein expression profiles on a cohort of 20 patients. Additional validation on a larger cohort of patients is required.

1446 Applying Computer Assisted Process Modeling To Improve Anatomic Pathology Workflows.

DS McClintock, RE Lee, CG Oberg, TM Gudewicz, JR Gilbertson. Massachusetts General Hospital, Boston.

Background: Anatomic Pathology (AP) labs are complex entities, a fact easily recognizable once attempts are made to map out the tens to hundreds of possible workflow processes involved in the daily preparation and processing of specimens. In areas outside of medicine, there are many computer assisted business process

management and workflow modeling techniques available to help break down this complexity, reduce redundant processes, and improve efficiency. However, to date, there has been minimal application of these techniques to the pathology laboratory.

Design: Multiple business process management software applications were considered with two primary software solutions chosen to describe the workflow processes in the MGH Anatomic Pathology laboratories. Surgical pathology accessioning, grossing, and histology; cytology and autopsy workflow processes were initially charted with their respective domain experts using Microsoft Visio 2007. The completed workflow charts then were imported into iGrafx Process (Corel) and estimated time data inserted for each process step. Computer assisted process models with associated simulations were subsequently built in iGrafx Process in order to better identify potential trouble areas.

Results: Over the course of four months (05-09/2010), 29 workflow process maps were created (7 AP master lab processes and 22 AP lab sub-processes), with an additional 35 AP lab sub-processes queued for completion (sample flowchart, figure 1).

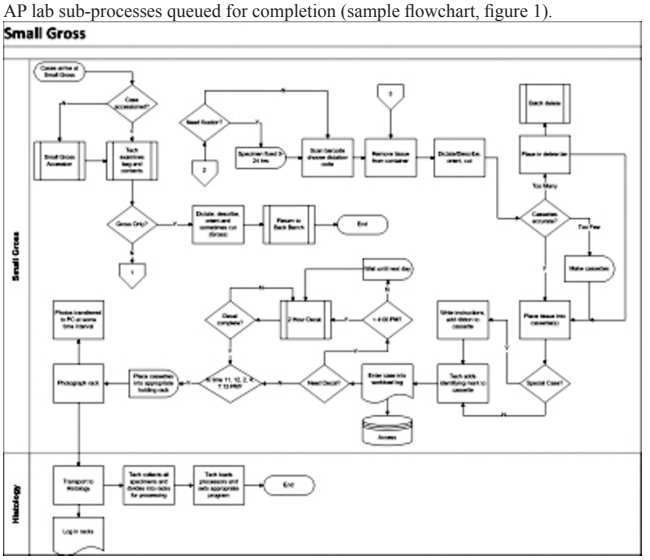

Computer assisted simulation of workflow process models is ongoing, with a sample simulation provided (figure 2).

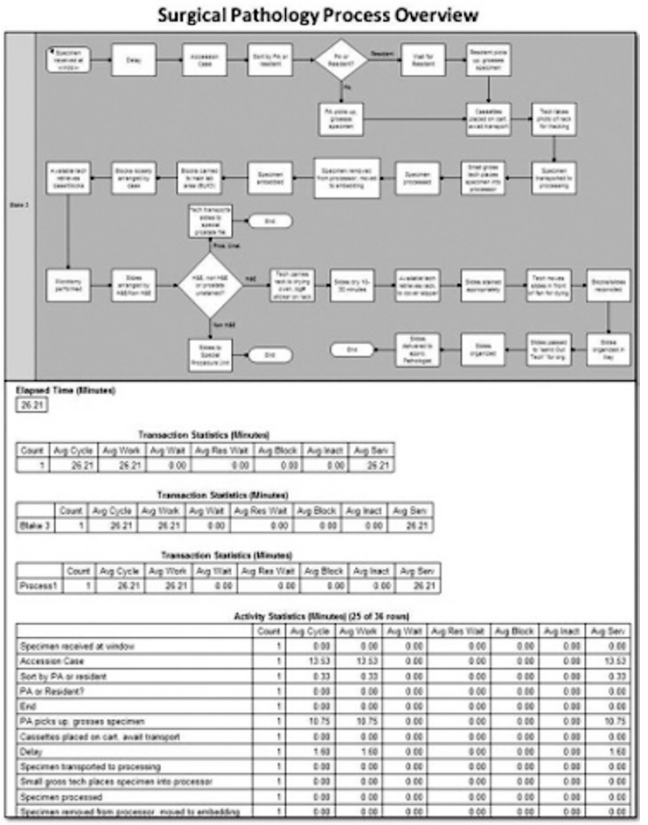

Conclusions: Improving AP laboratory processes is a constant challenge and requires a solution that meets the ever expanding complexity of modern pathology practices. As more efficiency is demanded from limited resources, computer assisted process modeling of AP workflows will not only easily identify problem areas, but also allow for constant adjustment of the workflow in order to achieve the desired results.

1447 Voice Recognition Technology: Experience with Implementation and Impact on Work Flow and Turn around Time.

T Pal, KA Dasilva, M Singh. Stony Brook University Medical Center, NY.

Background: There have been limited studies comparing the use of voice recognition technology (VRT) with transcription services for surgical pathology. The purpose of this study is to determine the feasibility and impact of the transition from a transcriptionist based service to VRT.

Design: At our institution, we have recently evaluated VRT in a phased manner for gross descriptions and later for case sign out, on the general and subspecialty surgical pathology services. Prior to that, we used transcriptionists to generate reports from either dictated tapes or handwritten notes. Initially, VRT was used by the residents and the pathologist assistant exclusively for dictating gross descriptions. After a pilot study of the effectiveness of VRT with case sign out, VRT was implemented for both grossing and final reports without the involvement of transcriptionists. We retrospectively compared the turn around time over an 8 month period before and after the introduction of VRT. The number of amendments generated for typographical errors was compared over the same time periods. Its impact on work flow, staffing and resident education was evaluated.

Results: 73% of total cases had the final diagnoses dictated using VRT during the 8 months it was evaluated. The average TAT for the 8 months without VRT usage was 3.67 days, and it decreased to 2.67 days in the corresponding 8 months after VRT was implemented (a 27% improvement). The portion of cases signed out in less than one day improved from 26.8% to 36.5% since VRT. When evaluating amendment rates for typographical errors no increase was identified related to the use of VRT. Informatics follow up on a regular basis has resulted in a smooth implementation both for grossing and final reports. Use of templates and synoptic reports was facilitated with VRT. The transcription staff was reassigned duties to further assist the department in improving work flow. Resident satisfaction was high.

Conclusions: Through the use of VRT, a significant improvement in TAT is noted. VRT allows for a seamless workflow where cases are signed out immediately after the slides are reviewed. This also has an added positive impact on competency-based resident education and permits graduated responsibility as residents are now able to participate in the full process of generating reports and the release of final reports by the pathologist as their cases are signed out.

1448 Use of Mobile High Resolution Device for Remote Frozen Section Evaluation of Whole Slide Images.

JP Ramey, K Fung, LA Hassell. Oklahoma University Health Sciences Center, Oklahoma City; Oklahoma City Veterans Affairs Medical Center, OK.

Background: Mobile, internet-capable, high resolution viewing devices (MVD) coupled with whole slide images (WSI) create a new paradigm for pathology consultation. Validation of results from use of these devices may be important for practitioners and regulators. We evaluate the potential use of MVD in frozen section (FS) analysis.

Design: A series of 72 consecutive cases with FS requests were selected for potential study. FS slides were scanned using an Aperio Scanscope scanner at 20x magnification. Scan times were recorded. All materials utilized in the FS consultation including gross images and descriptions, clinical information, cryostat sections and cytologic preparations were catalogued with the images and available to reviewers via MVD. A sample of WSI FS cases were presented to 3 pathologists for diagnosis on an iPad MVD using the InterpathHD application accessing the server running Aperio Spectrum software. Times to diagnosis were noted. The WSI FS results were compared to original reported and final diagnosis to derive kappa values. Cases with discrepancies were subjected to further consensus review of the original glass slides.

Results: Scan times averaged two minutes 15 seconds/case. Evaluation times averaged two minutes 29 seconds/slide. Complete concordance between initial FS diagnosis and that rendered via MVD was 89%. Minor discrepancy in WSI diagnosis and initial FS diagnosis that would not have impacted therapy at the time was observed in the remaining 11% of cases. The kappa statistic for this series was 0.83. Use of the InterpathHD application on the iPad presented challenges to users related to the movement of the slide at higher magnifications. Users were unable to smoothly navigate the image at high magnification, but were required to revert to a low magnification before they could locate another area to examine at high power.

Conclusions: Image fidelity and resolution make the iPad potentially suitable for WSI evaluation for diagnostic purposes. An acceptable level of accuracy is attainable for FS interpretation. The user interface may account for more rapid interpretation capability that that reported for similar processes using standard interface techniques. But while technically possible to obtain acceptable results, use of the iPad with InterpathHD to view WSI is not easy. The obstacle to examining the full slide at intermediate magnification and continuous areas at high magnification could introduce frustrations and delays or errors.

1449 The Value of Telepathology during Intraoperative Diagnosis of Pediatric Neuropathology.

AG Saad, SG Sharma, M Gokden. Arkansas Children's Hospital, Little Rock; University of Arkansas for Medical Sciences, Little Rock.

Background: Telepathology is a rapidly evolving field of digital pathology, particularly important for rapid expert opinion or assistance by a specialist during frozen section (FS). The aim of this study was to evaluate the accuracy and maneuverability of telepathology as a tool in seeking expert opinion in pediatric neuropathology. To the best of our knowledge, the value of telepathology in pediatric neuropathology has not been studied before.

Design: The study included primary central nervous system tumors received in the last 5 years. The cases were reviewed by two pathologists; the neuropathologist at the primary

site operated the microscope and the neuropathologist at the other center analyzed the cases while communicating on phone. The telepathology system comprised of Nikon's Eclipse 55i microscope and Nikon's digital camera DS-L2. The data collected were: time taken to render the diagnosis, types of challenges during this process, and when applicable, reasons and types of discrepancy. All slides were reviewed for accuracy of diagnosis.

Results: The search yielded 38 cases- 18 cases with their corresponding FS and 20 cases with no FS. Final diagnoses were: 12 gliomas, 6 meningiomas, 6 ependymomas, 5 medulloblastomas, 1 choroid plexus papilloma, 1 schwannoma, 1 hemangioblastoma, 1 cavernous hemangioma, 1 papillary craniopharyngioma, 2 subependymomas, 1 mucormycosis, and 1 Langerhan's cell histiocytosis. The average time taken to analyze each frozen case was 52 seconds (range: 19–180 seconds). Only one FS case (gemistocytic astrocytoma) had a discordant diagnosis with the final diagnosis (ependymoma) because of the absence of diagnostic area on the frozen section. The median time and standard deviation (in seconds) taken to diagnose cases were: medulloblastoma (94.5 ±3.5), gliomas (67±8.4), meningiomas (67±0.7), ependymoma (95 ±37.47), choroid plexus papilloma (45), schwannoma (53), hemangioblastoma (38), cavernous hemangioma (28), papillary craniopharyngioma (16), subependymomas (27), mucormycosis (26), and Langerhan's cell histiocytosis (60).

Conclusions: The diagnosis of FS using telepathology technology system proved to be a great asset in seeking expert opinion during FS interpretation or to seek second opinion in challenging cases with near perfect concordance rate. A potential important role for this technology would be to assist remote and/or understaffed hospitals during interpretation of FS.

1450 Reduction of Anatomical Pathology Slide Mislabel Rate Due to Implementation of Barcoding at Two Tertiary Care Hospitals.

G Sharma, A Piccoli, SM Kelly, LT Wiehagen, L Pantanowitz, AV Parwani. University of Pittsburgh Medical Center, PA.

Background: Manual entry of case numbers in the pathology laboratory information system to generate labels can lead to mislabeling of pathology specimens and their derivatives (blocks, slides etc.). Two dimensional (2D) bar coding technology has emerged as a viable technology for use in anatomical pathology laboratories. Benefits include accurate data entry when bar codes are scanned, asset tracking with routing, and a streamlined workflow. The aim of this study was to determine the effect of barcoding at different hospitals in reducing the slide mis-label rate.

Design: Barcoding was implemented in the histology laboratories at Hospital A (400+ beds, around 25,000 surgical pathology cases accessioned annually) followed by Hospital B (900+ beds, around 50,000 surgical pathology cases accessioned annually). A 2D Datamatrix barcode standard was integrated with the anatomical pathology laboratory information system (CoPath version 3.2; Cerner DHT, Kansas City, MO). Bar code printers (Shandon Microwriter; Thermo Scientific, Waltham, MA and GDKV2-C; General Data Corporation, Cincinnati, OH) for cassettes were installed at grossing stations and barcode printers for slide labels (Cognitive Cxi; CognitiveTPG, Lincolnshire, IL) using chemical resistant adhesive labels (StainerShield XT, General Data Corporation, Cincinnati, OH) were installed in the histology laboratory. Bar code scanners (Symbol DS 6607 and 6707; Motorola Corporation, Schaumburg, IL) were placed in the accessioning area, gross room, histology laboratory and at pathologists' workstations. The mislabeled slide rate before and after bar code implementation was compared.

Results: Implementation at Hospital A spanned 12 months (March 2008 to March 2009) where the rate of mislabeled slides decreased from 2.5 slides/month (pre-barcoding) to 0.58 slides/month (post barcoding).Implementation at Hospital B spanned 7 months (January 2009 to July 2009), where the rate of mislabeled slides decreased from 4.25 slides/month (pre-barcoding) to 2.74 slides/month (post-barcoding implementation).

Conclusions: Successful implementation of barcoding in anatomic pathology practice is best accomplished in a phased manner. Experience gained with initial implementation at a smaller laboratory decreases the implementation time at a larger laboratory. Our data show that 2D barcoding of slides can help significantly reduce mislabeling errors, even in complex anatomical pathology laboratories, and thereby improve patient safety.

1451 Diagnosing Endometrial Carcinoma via Computer-Assisted Image Analysis.

R Sivalingam, G Somasundaram, A Ragipindi, A Banerjee, AM Truskinovsky. University of Minnesota, Minneapolis.

Background: The diagnosis of endometrial endometrioid carcinoma is based primarily on architecture. We investigated whether endometrial carcinoma can be distinguished from proliferative endometrium using 2 methods of computer-assisted analysis, 1) region covariance descriptors and 2) discriminative dictionaries.

Design: We used 4 images each of H&E-stained sections of 2 diagnostic classes, proliferative endometrium and well-differentiated endometrioid carcinoma of the endometrium, scanned at x50 magnification on a digital slide scanner.

In the first method, an image region is represented using the covariance matrix over features in the region. Test image patches are classifi ed via k-NN classi fication using a geodesic distance measure over covariances. From the images in each class, we randomly sampled 100 k x k blocks from manually demarcated diagnostic regions in each image. We used 2 types of covariances:

C_{wave}: 40 x 40 covariances computed over the responses of 10 Daubechies wavelet filters;

C_{si}: 8 x 8 covariance descriptors computed over spatial (x, y, ρ, θ) and intensity I, I_x, I_y, $\sqrt{([I_x]^2 + [I_y]^2)}$ features.

We ran 2 types of cross-validation, a) 10-fold cross-validation on the entire dataset and b) image-wise cross-validation to test performance on unseen images, where we randomly select one test image from each class, using the rest for training.

In the second method, we vectorize $\sqrt{n}$ x $\sqrt{n}$ image patches into n-vectors, and a representative dictionary is learned for vectors from each class, under the constraint that each vector can be reconstructed by a sparse subset of the dictionary. The discriminative power lies in the fact that the dictionary from one class performs poorly at reconstructing patches from the other class. 32 x 32 patches were extracted from images of each class and discriminative dictionaries were learned using 12000 labeled training patches. Then three-fold cross-validation was performed.

Results: For the first method, the accuracy of the classification of images into proliferative endometrium and carcinoma was 96-98% for 10-fold cross-validation and 94-96% for image-wise cross-validation. The accuracy was highest for 200 x 200 blocks, showing that this is a discernible scale for classi fication. C_{si} performed slightly better than C_{wave}, though the di fference was not statistically signi ficant. For the second method, the overall classi fication accuracy was 60-80%.

Conclusions: Computer-assisted analysis can be used with high accuracy to distinguish well-differentiated endometrioid carcinoma from proliferative endometrium.

1452 Quantifying Gland Morphology for Computerized Prostate Cancer Detection and Gleason Grading.

RE Sparks, A Madabhhushi. Rutgers University, Piscataway, NJ.

Background: Observer variability between expert pathologists when assigning Gleason grade is high, particularly distinguishing Gleason patterns 3 from 4. Consequently there is need for decision support system that having extracted subtle, quantitative image descriptors can help distinguish intermediate Gleason patterns.

Gleason patterns differ subtlety in their in their gland morphology and nuclear structure, with pattern 3 glands being larger and more distinct compared to pattern 4 glands. Similarly benign prostate glands tend to be larger with distinct lumen and orderly nuclei Compared to malignant glands which tend to be small with indistinct lumen and irregular nuclei. In this work we present a novel scheme for extracting quantitative descriptors of gland morphology that can be used to distinguish (a) intermediate Gleason grade patterns, and (b) malignant and benign prostate areas.

Design: We present novel Explicit Shape Descriptors (ESDs) for modeling gland morphology. The method involves (a) modeling gland shape (via the medial axis transform as seen in Figure 1), (b) pairwise comparison between fitted shape models, (c) dimensionality reduction to obtain ESDs, and (d) a support vector machine classifier to distinguish (i) Gleason patterns, and (ii) benign and malignant areas.

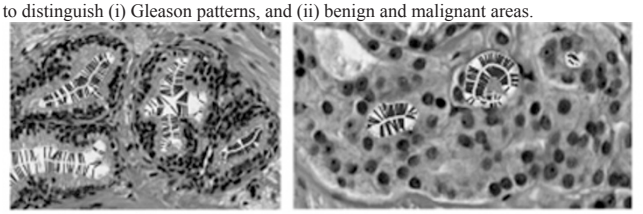

Figure 1. (a) Medial axis transform fit to benign glands and (b) medial axis transform fit to Gleason pattern 3 gland. Note how the medial axis transform differs between the two types of glands.

Results: An expert pathologist assigned a Gleason pattern to 120 regions of interests (ROIs) from 58 prostate biopsy studies (serving as ground truth). 888 glands were selected from benign (24 ROIs, 93 glands), Pattern 3 (67 ROIs, 748 glands), and 4 (11 ROIs, 47 glands) ROIs.

Table 1

Task	Malignant v. Benign	Pattern 3 v. Other (Benign, Pattern 4)	Pattern 4 v Other (Benign, Pattern 3)	Pattern 3 v Pattern 4
AUC	0.84±0.09	0.81±0.03	0.85±0.09	0.87±0.11

Area under the ROC curve (AUC).

Table 1 displays the AUC for four classification tasks, which is over 0.80 in all tasks.

Conclusions: We presented explicit shape descriptors for modeling gland morphology in order to distinguish (a) benign and malignant glands on needle cores, and (b) subtle differences between Gleason patterns 3 and 4. Future work will involve combining ESDs with architectural features for improving our Gleason grading classifier.

1453 A Content-Based Image Retrieval System for Digitized Prostate Histopathology.

A Sridhar, S Doyle, A Madabhushi. Rutgers University, Piscataway, NJ.

Background: In a content-based image retrieval system (CBIR) system, the user inputs a query image and the system outputs images from the database that are most similar to the query image. Such a system in the context of prostate cancer pathology would be an invaluable educational, research, and clinical tool for pathologists. For instance, approximately 1 million prostate cancer needle core biopsies, with a corresponding 15 million prostate tissue samples, are generated annually. However, only 1 million samples are positive for cancer. The CBIR companion tool can help reduce the time pathologists spend looking at benign samples, allowing them to focus on the suspicious samples. Our new CBIR system utilizes a weighted distance metric (WDM) and we apply it to the problem of distinguishing benign from malignant prostate cancer biopsy images.

Design: H&E stained prostate histopathology images were obtained from 58 patients and 14 texture features were extracted from each image. Each texture feature in conjunction with a Bayesian classifier was used to build a weak learner. The machine learning algorithm Adaboost was then used in conjunction with these weak learners to learn feature weights which resulted in maximum discriminability between the benign and malignant classes in a training set. The weights obtained were used in conjunction with the Euclidian distance metric resulting in a WDM. The WDM is then used to build a CBIR system to retrieve database samples that are most similar to the query image.

Results: Precision-Recall (PR) curves were used to evaluate the WDM-CBIR and compared against a CBIR system that used the Euclidian distance metric (EDM-CBIR) with the same texture features. Figure 1a clearly shows that our WDM-CBIR outperformed the EDM-CBIR on a cohort of 58 prostate cancer studies. The average area under the curve for the WDM-CBIR was 0.95 compared to 0.72 for the EDM-CBIR.

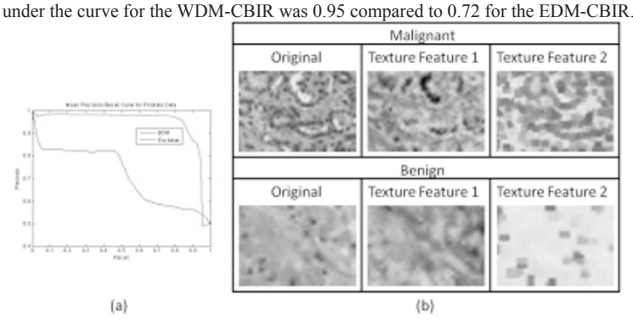

Figure 1: (a) PR Curves for WDM and EDM CBIR systems evaluated on prostate biopsy studies. (b) Representative examples of malignant and benign regions with corresponding texture representations.

Conclusions: We introduced a new WDM-CBIR system that differentially weights individual image attributes based on their discriminatory performance. WDM-CBIR outperformed the EDM-CBIR on 58 prostate cancer studies. WDM-CBIR can be extended and applied to other domains within digital pathology.

1454 Telecytopathology for Rapid Preliminary Diagnosis of Ultrasound-Guided Fine Needle Aspiration of Thyroid Nodules.

IN Swati, R Izquierdo, R Kasturi, KK Khurana. SUNY Upstate Medical University, Syracuse, NY.

Background: Onsite evaluation of ultrasound-guided fine needle aspiration (USGFNA) is essential to procure adequate samples and provide initial assessment. We present our experience with onsite evaluation of USGFNA using telecytopathology.

Design: Real time images of Diff Quik stained cytology smears were obtained with an Olympus Digital camera attached to an Olympus CX41 microscope and transmitted via ethernet by cytotechnologist to a pathologist who rendered preliminary diagnosis while communicating with onsite cytotechnologist over the phone. Accuracy of preliminary diagnosis was compared with final diagnosis, retrospectively. Kappa statistic was used to compare agreements between telecytopathology preliminary diagnoses versus final diagnoses.

Results: A total of 51 patients (mean age 48.9 yr) underwent USG-FNA of 65 thyroid nodules. Preliminary diagnoses of benign, suspicious/ malignant and unsatisfactory were 77%, 5% and 18% respectively. Of the 50 cases initially reported as benign all remained benign on the final cytology. All suspicious / malignant cases on initial cytology corresponded with a malignant diagnosis on final cytology. Of the 12 cases that were initially interpreted as unsatisfactory only 2 were reclassified as benign on final diagnosis. There was excellent agreement between telecytopathology and final cytologic evaluation (Kappa value 85%). Presence of additional material on pap stained slides was the main reason for discrepancy accounting for two discrepant cases in the unsatisfactory category.

Conclusions: This retrospective study demonstrates onsite telecytopathology evaluation of thyroid USG-FNA is highly accurate compared with final cytologic evaluation. It allows pathologists to use their time more efficiently and makes onsite evaluation at a remote site possible.

Kidney

1455 The Renal Distribution of Iron (Fe) in Primary Hemochromatosis: An Autopsy Study.

V Ananthanarayanan, S Meehan, A Chang. University of Chicago, IL.

Background: The distribution of iron (Fe) within the renal parenchyma of patients with primary hemochromatosis has not been studied. We conducted this study to determine the spectrum of Fe distribution in autopsy kidneys in the setting of primary hemochromatosis. We also evaluated whether the presence of the H63D or C282Y mutations, the most common mutations in hereditary hemochromatosis, resulted in a difference in iron distribution in the kidneys of affected patients.

Design: We identified 12 cases of hemochromatosis in our pathology database from 1993-2010, after excluding cases of hemosiderosis and secondary hemochromatosis. H&E and Prussian blue stain were analyzed and the distribution of Fe in the various compartments of the renal parenchyma was assessed. These findings were correlated with the available clinical and mutation data (H63D and C282Y).

Results: Of the 12 cases of primary hemochromatosis, there were 8 males and 4 females with an average age of 54 years (range: 32 to 73 years). Eight patients had histologically proven cirrhosis while 4 patients had increased Fe deposition in the hepatocytes. In the kidneys, there typically was more staining for Fe in the cortex than the medulla. Within the cortex, Fe was noted in the glomeruli, proximal convoluted tubules (PCT) and distal nephron segments. In most cases, the staining in the distal nephron segments, when present, was more intense than the PCT. Podocytes and parietal epithelial cells were the primary cells in glomeruli with Fe, but no mesangial or glomerular endothelial staining was identified. One case showed the presence of Fe in only glomeruli limited to the podocytes. Few cases had additional rare interstitial and endothelial staining. Furthermore, patchy staining of the glomerular basement membranes in globally sclerotic glomeruli, Bowman's capsules and tubular basement membranes was also noted in a subset of cases. In the four cases where mutation data was available, no difference in Fe distribution was observed.

Conclusions: This is the first study to describe the distribution of Fe in autopsy kidneys of primary hemochromatosis patients. Most cases showed a predominant staining pattern in the cortex with a greater distribution in the distal nephron segments. Regardless, of the involved compartment, Fe deposition was patchy and irregular. The persistence of iron deposition in the podocytes could be due to their terminal differentiation, but this would require further study.

1456 Identification of a Potential Marker of Glomerular Fibrogenesis in Childhood Nephrotic Syndrome.

MM Cajaiba, R Ayoob, R Houston, SI Bastacky, P Baker. Nationwide Children's Hospital, Columbus, OH; University of Pittsburgh, PA.

Background: Minimal change disease (MCD) and focal segmental glomerulosclerosis (FSGS) are the major causes of pediatric nephrotic syndrome (NS). Most MCD cases respond to steroids, whereas FSGS tends to be resistant and progress to global sclerosis leading to chronic renal disease. The reversible nature of MCD is thought to reflect transient podocyte damage due to increased circulating cytokines, whereas FSGS would correspond to irreversible podocyte damage with activation of TGF-β-mediated apoptosis and fibrogenesis. Markers of fibrogenesis that could help to define the pathogenesis and prognosis in these cases have not been clearly identified. One of the downstream targets of TGF-β signalling is Sox9, a transcription factor involved in normal skeletal development and pathological fibrogenesis. Recent experimental studies showed increased levels of both Sox9 and TGF-β mRNA in FSGS, and increased glomerular collagen IV accumulation triggered by TGF-β-induced Sox9 expression. The aim of this study is to investigate Sox9 as a potential indicator of glomerular fibrogenesis in NS.

Design: 29 renal needle biopsies performed in children with NS were selected; 15 were diagnosed as FSGS and 14 as MCD. 10 renal biopsies from healthy living transplant donors were used as normal controls. Immunohistochemical stains with an antibody against Sox-9 were performed on representative slides from each case. Specimens with sampling of 5 or more glomeruli were considered adequate. Sox9 nuclear staining was recorded as positive/negative in glomeruli (mesangial cells/podocytes), and as percentage of stained cells in parietal and tubular epithelial cells (PEC/TEC).

Results: Ages ranged from 1-18 years, with 14 males and 15 females. 5 cases (3 FSGS and 2 MCD) were excluded due to sampling inadequacy. None (0/10) of the normal controls showed glomerular staining. 7/12 (58.3%) FSGS cases had positive glomerular staining (seen in segmentally sclerotic and non-sclerotic glomeruli) versus 1/12 (8.3%) MCD cases (p=0.0136). Sox9 stained 0-10% of TEC and PEC in all controls (100%) and most MCD (67%), and 10-50% in most FSGS cases (67%).

Conclusions: Glomerular Sox9 expression was significantly more frequent in FSGS than MCD, suggesting a potential use for this protein as a diagnostic/prognostic marker of fibrogenesis in NS. A larger patient sample is needed to confirm these observations, to establish a possible relationship between Sox9 staining and poor outcome in MCD, and an association between tubular Sox9 staining and chronic parenchymal changes.

1457 Clinical Implications of Polyomavirus-Associated Nephropathy after Renal Transplantation.

HP Cathro, JC Gardenier, CD Sifri, DS Keith, RG Sawyer, KL Brayman, H Bonatti. University of Virginia, Charlottesville; Vanderbilt University, Nashville, TN.

Background: BK virus nephropathy (BKVN) develops in ~5% of renal transplants (RT), causing graft loss in 15-80% of cases within 5 years. Most studies suggest that the majority of BKVN occurs during the first post-transplant (PT) year. We noticed an increasing number of cases of late-onset BKVN and conducted a retrospective study.

Design: All renal specimens from patients with biopsy-proven BKVN from 2000-2009 at a single institution were reviewed.

Results: Of 846 RT recipients, 18 had biopsy-proven BKVN (2.1%), 4 of whom had also received pancreatic transplants. The median age of 12 males and 6 females was 52.2 yr (range 27.9-63.8 yr), and the median time PT was 20.1 mn (range 3.2-80.4 mn), with only 4 or 22%, <1 yr out. Fourteen patients were on standard immunosuppression (IS). Screening for BK virus was erratically administered due to geographical/logistical constraints. Five patients had prior biopsy proven episodes of acute rejection and 13 patients (72%) had received intensive prior IS, usually for acute rejection (n=10) or for subsequent pancreas transplantation. Fourteen patients were treated with antiviral therapy, +/- IVIG, +/- IS taper, and single patients were treated with IVIG or IS taper alone. One patient died after returning to dialysis, and 17 were alive at an average of 3.4 yr follow up. Seven of these had returned to dialysis (41%), and 5 had a serum creatinine >2 mg/dL (29%). Only 5 patients had good graft function (29%).

Conclusions: Retrospective analysis of BKVN at a single institution during the current IS era demonstrated 78% of cases occurring after the first PT year, and 39% after the second PT year. Inconsistent screening and over-IS may be playing a role. The poor outcome of 72% of the BKVN cases is in part due to late diagnosis at a severe stage of disease. Late onset BKVN is an underrecognized cause of graft loss and dysfunction, and rigorous screening followed by tapering of IS on positive testing, should be emphasized beyond the first year post-transplantation.